

## Short-wavelength infrared (1.3–2.6 $\mu\text{m}$ ) observations of the nucleus of Comet 19P/Borrelly

L.A. Soderblom,<sup>a,\*</sup> D.T. Britt,<sup>b</sup> R.H. Brown,<sup>c</sup> B.J. Buratti,<sup>d</sup> R.L. Kirk,<sup>a</sup> T.C. Owen,<sup>c</sup> and R.V. Yelle<sup>c</sup>

<sup>a</sup> *United States Geological Survey, 2255 N Gemini Drive, Flagstaff, AZ 86001, USA*

<sup>b</sup> *Department of Physics, The University of Central Florida, PO Box 162385, Orlando, FL 32816-2385, USA*

<sup>c</sup> *Departments of Planetary Sciences and Astronomy, University of Arizona, 1629 E. University Boulevard, Tucson, AZ 85721, USA*

<sup>d</sup> *Jet Propulsion Laboratory, California Institute of Technology, 4800 Oak Grove Drive, MS 183-402, Pasadena, CA 91109, USA*

<sup>e</sup> *Institute for Astronomy, University of Hawaii, 2680 Woodlawn Drive, Honolulu, HI 96822, USA*

Received 25 November 2002; revised 24 July 2003

### Abstract

During the last two minutes before closest approach of Deep Space 1 to Comet 19P/Borrelly, a long exposure was made with the short-wavelength infrared (SWIR) imaging spectrometer. The observation yielded 46 spectra covering 1.3–2.6  $\mu\text{m}$ ; the footprint of each spectrum was  $\sim 160 \text{ m} \times$  width of the nucleus. Borrelly's highly variegated and extremely dark 8-km-long nucleus exhibits a strong red slope in its short-wavelength infrared reflection spectrum. This slope is equivalent to J–K and H–K colors of  $\sim 0.82$  and  $\sim 0.43$ , respectively. Between 2.3–2.6  $\mu\text{m}$  thermal emission is clearly detectable in most of the spectra. These data show the nucleus surface to be hot and dry; no trace of  $\text{H}_2\text{O}$  ice was detected. The surface temperature ranged continuously across the nucleus from  $\leq 300 \text{ K}$  near the terminator to a maximum of  $\sim 340 \text{ K}$ , the expected sub-solar equilibrium temperature for a slowly rotating body. A single absorption band at  $\sim 2.39 \mu\text{m}$  is quite evident in all of the spectra and resembles features seen in nitrogen-bearing organic molecules that are reasonable candidates for compositional components of cometary nuclei. However as of yet the source of this band is unknown.

© 2003 Elsevier Inc. All rights reserved.

**Keywords:** Comet; Temperature; Thermal emission; Imaging spectrometer; Short-wavelength infrared; SWIR; JHK color; Nitrogen-bearing organic molecules; H–K color; J–H color; Infrared spectra; Spectral absorption; Nucleus; Short-period comets; 19P/Borrelly; Borrelly; Deep Space 1

### 1. Introduction

The Deep Space 1 (DS1) spacecraft (S/C) passed about 2171 km from the Jupiter-family short-period Comet 19P/Borrelly on September 22, 2001. Built by NASA-JPL under the New Millennium Program, DS1 was the first spacecraft to demonstrate ion propulsion in deep space. This article describes analysis of 46 short-wavelength infrared (SWIR) spectra (1.3–2.6  $\mu\text{m}$ ) that were collected with the advanced-technology MICAS (Miniature Integrated Camera and Spectrometer) instrument (Soderblom et al., 2002). These are the first near-infrared spectra of a cometary nucleus acquired from the close flyby of a spacecraft. The encounter was close to the ecliptic plane and occurred only  $\sim 8$  days after perihe-

lion at a heliocentric range of 1.362 AU Nelson and Rayman (this issue) provide an overview of the DS1 Mission and the encounter with Borrelly.

MICAS was an integrated four-channel instrument in which two visible-wavelength cameras and two imaging spectrometers (infrared and ultraviolet) shared a single telescope (Soderblom et al., 2000). Table 1 in Soderblom et al. (this issue) lists the basic parameters of the MICAS channels; Fig. 1 shows the optical layout of the instrument. Of the four MICAS channels only the VISCCD (Visible-wavelength Charge Coupled Device) Imager and SWIR Imaging Spectrometer returned useful scientific data from the encounter. Unfortunately the detector for the UV Imaging Spectrometer failed soon after launch. The APS (Active Pixel Sensor) Imager had been configured for use on bright targets (Earth, Moon, Mars, Jupiter) and as such was too insensitive for the dim light levels from Borrelly's coma, jets, and surface. This article describes the observations ac-

\* Corresponding author.

E-mail address: [lsoderblom@usgs.gov](mailto:lsoderblom@usgs.gov) (L.A. Soderblom).

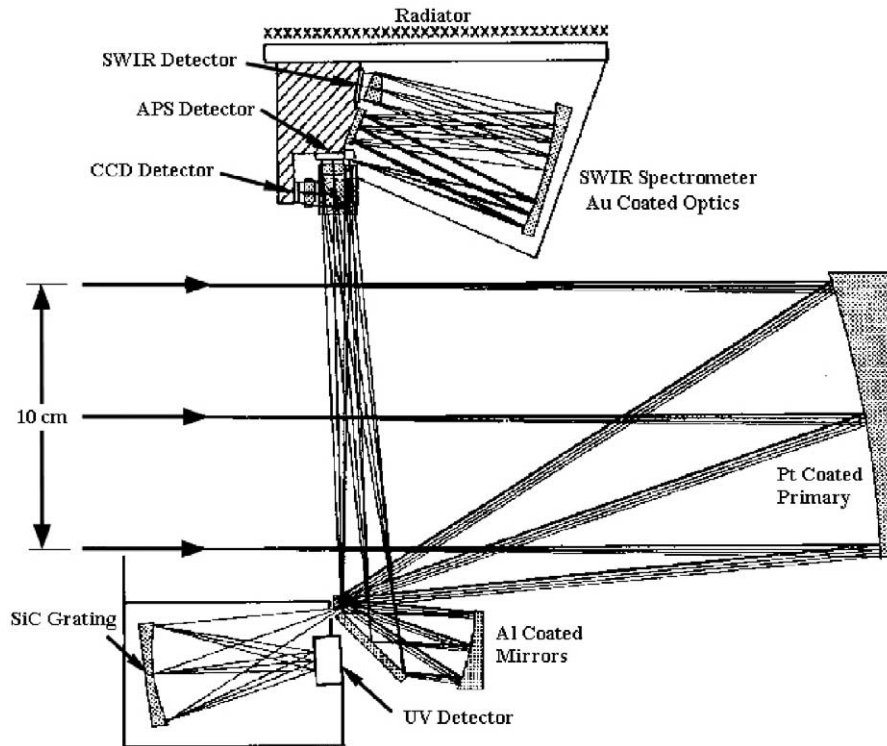


Fig. 1. MICAS optical layout. The integrated optical system used an off-axis Gregorian telescope. Its structure and optics were fabricated entirely out of silicon carbide (SiC). To preserve spectral performance over the wide wavelength range, a variety of coatings were used: Pt for the primary mirror, SiC for the UV alone, Al for combined VISCCD and SWIR, and Au for SWIR alone.

quired with the SWIR imaging spectrometer; results from the VISCCD camera channel are treated in a companion article (Soderblom et al., this issue).

MICAS was a close derivative of PICS (Pluto Integrated Camera Spectrometer) that was designed and demonstrated as an engineering model as a low-mass, low-power ( $\sim 7$  kg,  $\sim 7$  W) integrated instrument for the original Pluto Fast Flyby Mission (Beauchamp et al., 1994). The principal MICAS/PICS new technology was the use of SiC (silicon carbide) for a monolithic structure, multi-focal-plane optical bench, and multi-wavelength optics. This material was essential to realize very low mass and to achieve combined thermal and optical stability requirements. Silicon carbide has

- (1) very high stiffness-to-mass ratio and the strength to allow it to be thinned to reduce mass while retaining rigidity and exceptional optical performance, and
- (2) high thermal conductance and a very low coefficient of thermal expansion providing very high thermal stability.

Tests of the MICAS/PICS monolithic SiC structures, optical bench, and optics showed them to retain optical alignment to  $\sim 1/10$  wave over a broad range of temperatures, from ambient to cryogenic thermal environments (Beauchamp et al., 1994; Soderblom et al., 2000).

Although the full spectral range of the MICAS SWIR channel was  $1.0\text{--}2.8$   $\mu\text{m}$  (256 spectral samples, each

$0.007$   $\mu\text{m}$  wide), the region of the data with useful SNR (signal-to-noise ratio) is about  $1.3\text{--}2.6$   $\mu\text{m}$ . The MICAS SWIR channel was an imaging spectrometer that mapped a target simultaneously with 256  $54\text{-}\mu\text{rad}$  fields-of-view (FOV), generating a spectrum for each. At one end of the spectrometer slit a square aperture ( $2 \times 2$  mrad) was provided to observe point targets (stars and distant planets). Also a key element of the new technology contribution was the SWIR detector, an advanced Rockwell NICMOS-based infrared detector array, developed under the NASA Planetary Instrument Development and Definition Program (Beauchamp et al., 1994).

## 2. SWIR observational sequence for Borrelly

The near-encounter imaging sequence using the VISCCD camera lasted from about  $-87$  minutes up to about  $-2$  minutes from closest approach (C/A) to Borrelly (Soderblom et al., this issue). After the imaging sequence, during the last two minutes before C/A, long exposures (named IRSTREAK1.PDS and IRSTREAK2.PDS) were made with the SWIR imaging spectrometer with the hope that the nucleus would traverse the slit. The SWIR observations had to be placed after the end of the VISCCD imaging sequences because the camera was used not only to collect scientific images, but also to continuously control the S/C (spacecraft) orientation in order to track the nucleus through the

encounter. Because the SWIR slit FOV is outside the VIS-CCD frame FOV, collecting SWIR spectra earlier in the near-encounter sequence would have required slewing the camera off the target during the imaging sequence; the risk was that the target might not be reacquired and all subsequent higher resolution images lost.

Fortunately the near encounter SWIR sequence was successful; the first SWIR observation (IRSTREAK1) captured the nucleus. This was a 28-s exposure commencing at  $-117$  s, that traversed the nucleus generating 46 spectra. The footprint of each spectrum is  $\sim 160$  m  $\times$  the width of the nucleus. The second observation was a 19.7-s exposure that started at  $-77$  s. While missing the nucleus the second observation is invaluable in validating dark level and removing effects of low-level scattered light.

The Borrelly flyby was chosen to be on the sunward side of the nucleus. This meant that MICAS would be viewing Borrelly in the down-sun direction during the near-encounter phase. This was important because the MICAS instrument was prone to contamination by solar stray light when the solar cone-angle is  $\sim 90^\circ$  or less. For example, at  $-80$  minutes, 15 observations of Borrelly were collected through the SWIR keyhole. These were heavily contaminated with stray light that, coupled with the very low brightness of Borrelly, made them unusable. The IRSTREAK1 observation remains the sole useful data set collected by the SWIR of Borrelly's nucleus.

### 3. SWIR characteristics, calibration, data reduction, and validation

The SWIR data were collected on a two-dimensional NICMOS detector consisting of  $256 \times 256$  HgCdTe elements. All the spatial-spectral images shown in this paper are oriented with the dispersion direction horizontal so that wavelength increases from left-to-right. In this orientation, the slit is vertical with the  $2 \times 2$  mrad keyhole at its top. The keyhole occupied lines 10 to 40 and the slit lines 40 to 256 on the detector. The NICMOS detector was divided into four  $128 \times 128$  quadrants that were read out in parallel, interleaved by pixel producing a single  $256 \times 256$  data frame. When a standard exposure was commanded, the device was read twice. First a "flush" frame was exposed for 112 ms and read in order to reset the detector and to provide an estimate the dark level. The device was then set to integrate for the selected exposure time (218, 437 ms, etc. by factors of  $\times 2$ ) and was again read out requiring an additional 112 ms. Because the device was not reset after the flush frame is read, the second readout contained a total integration of the selected exposure time plus 224 ms. Figure 2 shows an example of a raw image acquired during spectral radiometric calibration in the laboratory. The target used for this data set was collimated light through the SWIR slit from an Optronics broadband lamp used as a calibration standard. The dark bars at the bottom and right of each quadrant are

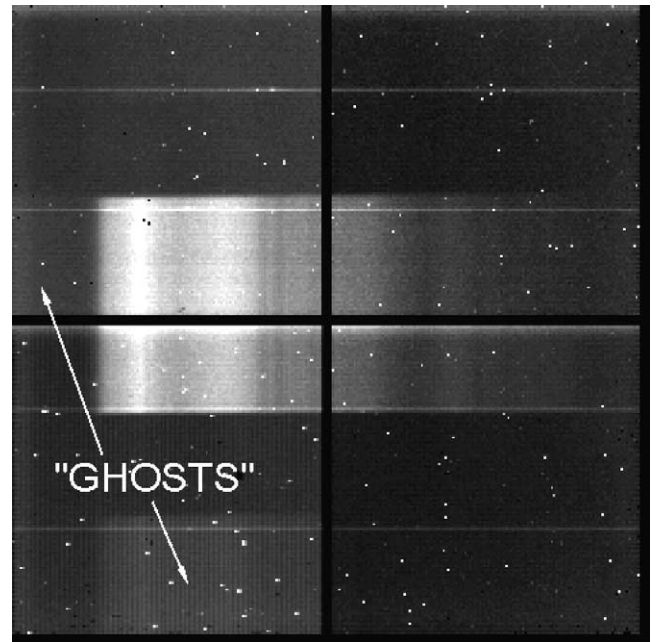


Fig. 2. Raw SWIR data frame from a laboratory light-transfer calibration sequence. Wavelength dispersion is left-to-right. The four framelets represent four  $128 \times 128$  quadrants of the SWIR NICMOS detector separated by dummy pixels (dark bars at middle, bottom and right). "Ghosts" are described in the text.

dummy pixels added by the readout electronics; they do not exist on the detector.

The calibration of the SWIR data is broken into two stages:

- (1) image processing corrections (those performed in detector-image-array format), and
- (2) spectral format corrections (those performed after the data have been converted to individual spectra).

Visible in Fig. 2 are fixed patterns (horizontal bright lines and bright pixels) that exist primarily in the dark level frames. Another pattern is visible in Fig. 2 that we refer to as "ghosts." The NICMOS detector readout was pixel-interleaved by quadrant. The electronics had a defect in that the capacitive time-constant for decay of the analog signal was of the order of the time between reads. This caused a fraction of the signal in one quadrant to be carried into the next, causing a ghost in the adjacent quadrant. These electronic ghosts travel counterclockwise from quadrant to quadrant and must be removed prior to any other processing step. It was found that the ghost contribution was very close to a constant fraction of the signal in the source quadrant (different fractional constants, however, between 0.06 and 0.16 for each quadrant). These levels were checked in flight and slightly revised. The ghosts are removed by simple subtraction of a fraction of the signal in each quadrant from the quadrant read next (noting however that the ghost traveling from quadrant 4 in upper left to quadrant 1 in the lower left, are also spatially shifted).

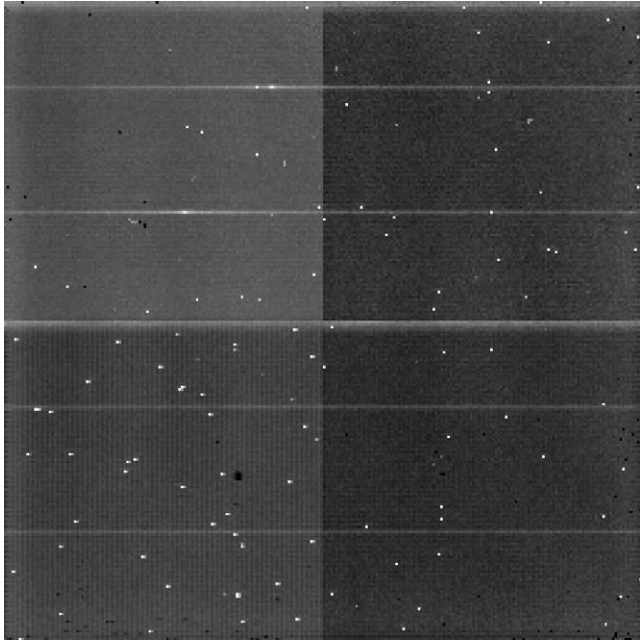


Fig. 3. Dark-level frame derived from flush and expose frames of Fig. 2. Dummy pixels have been removed.

Following removal of electronic ghosts, the next step is to estimate the dark level contribution. We do not simply subtract the flush frame from the expose frame but explicitly solve for and remove the dark level image, for several reasons. First this allows the flush frame to be used by itself as an observational data set. In some cases, in particular keyhole observations of Mars (Soderblom and Yelle, 2001), only the flush frames were collected so that independent estimates of dark background were required. Second, there can be spatial drift between the flush and expose frames resulting in misregistration. Solution for the dark level component is quite straightforward involving extrapolation of the flush frame and expose frames to zero-exposure. Figure 3 shows the dark level frame extrapolated from flush and expose frames of the data set in Fig. 2.

The data in Fig. 2 are part of a preflight light transfer sequence to document the linearity of the SWIR detector. Figure 4 shows a composite of light transfer curves (LTC) collected for an ensemble of detector elements distributed uniformly across one quadrant along with the model LTC used for calibration. As each quadrant exhibits a slightly different non-linearity and overall sensitivity, LTC models were derived for each quadrant.

The last correction applied in detector-image-array format is resampling to remove a small shear ( $\sim 1$  pixel across the 256 array; columns are left intact and simply shifted up-down) introduced by the off-axis optical design. Figure 5 was derived from the same data set of Fig. 2 and shows the result of the combination of ghost decontamination, dark background subtraction, correction for non-linearity, correction for sensitivity differences between quadrants, despiking to identify and remove “hot” and dead pixels, and correction for the small optical shear.

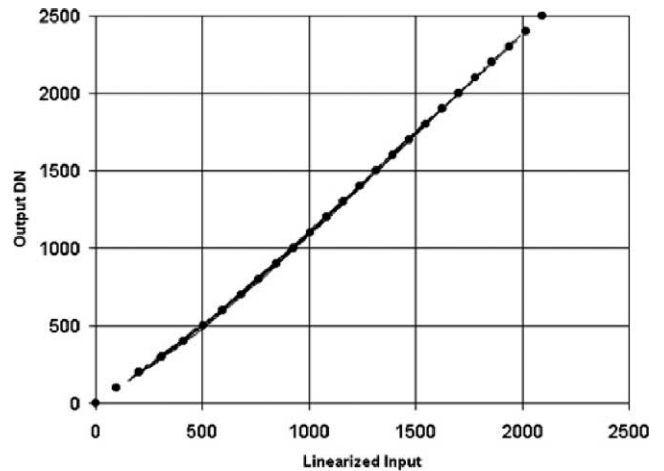


Fig. 4. Light transfer curve (LTC) showing a slightly non-linear but spatially uniform response for one NICMOS quadrant.

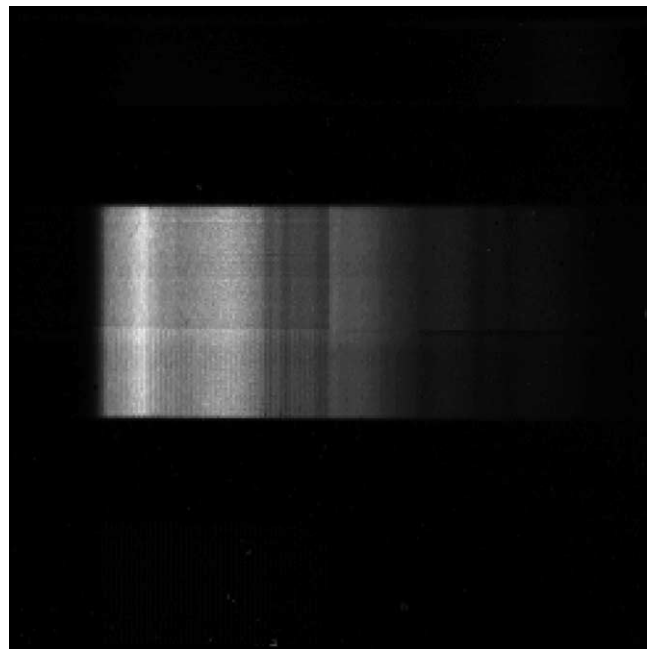


Fig. 5. Data frame of Fig. 2 after image-array correction procedures.

After image array corrections are completed the individual spectra are extracted and corrections applied in the spectral domain. This consists of wavelength calibration and correction for spectral throughput (the instrument’s spectral transform function). The output of the Optronics calibration lamp standard was carefully documented independently both in terms of wavelength and spectral radiance (Fig. 6). Although the full spectral range (spanning the detector) was 1.0–2.8  $\mu\text{m}$  with 0.007- $\mu\text{m}$  wide spectral elements, from Figs. 5 and 6 it is apparent that the useful spectral range of the instrument is about 1.3–2.6  $\mu\text{m}$ . The spectral wavelength calibration was updated using a combination of the positions of absorption features in the Optronics calibration lamp spectrum (Fig. 6) and of CO<sub>2</sub> bands in the martian spectrum acquired from DS1 in flight (Soderblom and Yelle,

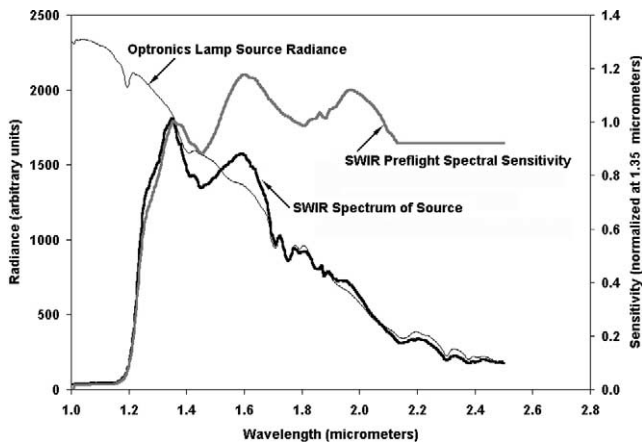


Fig. 6. Laboratory SWIR spectral response model derived from the MICAS SWIR measurement of the Optronics calibration source. This SWIR preflight spectral response function was arbitrarily set to a constant beyond  $\sim 2.1 \mu\text{m}$  due to low SNR of the available test data.

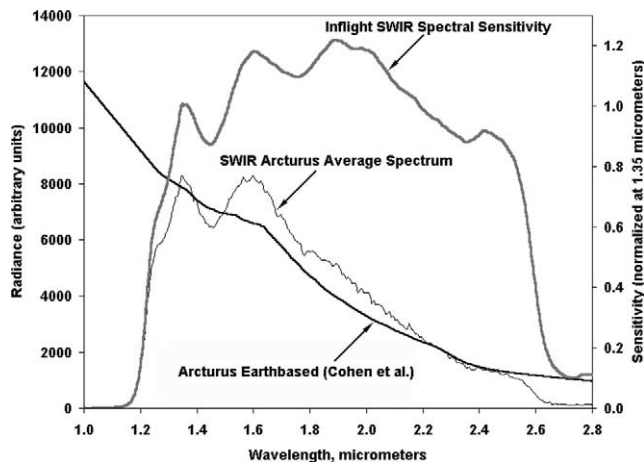


Fig. 8. MICAS SWIR spectral response derived from in-flight observations. Improved calibration was generated using DS1 in-flight observations of Arcturus compared to infrared flux measured telescopically by Cohen et al. (1995).

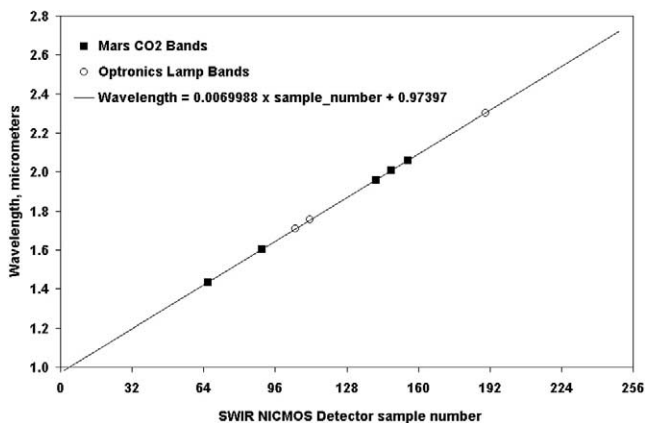


Fig. 7. Wavelength calibration. SWIR spectral sample as a function of wavelength was derived from a combination of laboratory observations of spectral absorptions (cf. Fig. 6) and in-flight observations of  $\text{CO}_2$  bands in the martian atmosphere.

2001). The wavelength calibration fit is given in Fig. 7 and is extremely close to the design parameters (shifted by only  $\sim 4$  spectral samples).

Figure 6 shows the spectral response derived pre-launch using an Optronics calibration lamp standard. The laboratory-based sensitivity model derived from this data was inadequate. At wavelengths beyond  $\sim 2.1 \mu\text{m}$  the SNR was too poor to provide a reliable estimate of the spectral response; hence a constant was arbitrarily adopted for that region in Fig. 6. Better spectral calibration data were acquired in flight from observations of Arcturus ( $\alpha$  Bootes) through the SWIR keyhole. The data were analyzed using Earth-based spectroscopic observations of Cohen et al. (1995). The results of this calibration (Fig. 8) validated the shorter wavelength part of the preflight calibration and provided much more reliable calibration of the instrument’s spectral sensitivity out to  $\sim 2.6 \mu\text{m}$ .

The calibration procedures described above were validated on SWIR spectra of Mars (Soderblom and Yelle,

2001). These data were acquired in-flight from DS1 during November 1999 when Mars was at a range of  $\sim 0.37$  AU from the S/C,  $\sim 1.38$  AU from the Sun, and at a solar phase angle of  $\sim 53^\circ$ . The martian season was northern Autumn (heliocentric longitude,  $L_s \sim 240^\circ$ ) with sub-S/C latitude  $\sim 18^\circ$  S and sub-solar latitude  $\sim 22^\circ$  S. MICAS returned 41 high-quality spectra through the SWIR keyhole during two full rotations of Mars (Fig. 9). Also shown in this figure is a model of the expected Mars spectrum (computed by one of us, RVY) that includes an optically thin haze (dust) uniformly mixed with the atmospheric gases. Atmospheric opacity was calculated line-by-line from the Hitran line listing. Parameters for the model were as follows:  $T_{\text{surface}} = 250$  K decreasing with altitude at  $0.5$  K/km;  $\text{CO}_2$  surface pressure = 4 mbar; CO and  $\text{H}_2\text{O}$  mole fractions = 0.001; haze particles optical properties {diameter =  $1.7 \mu\text{m}$ , size variance = 0.25, real index = 1.51, imaginary index = 0.0026}, column density =  $2 \times 10^6$ ; and Lambertian surface albedo = 0.2. The extraordinarily good agreement between the model calculation and the reduced MICAS SWIR spectra provides validation of the calibration data and procedures used here.

#### 4. Analysis of the Borrelly spectra

##### 4.1. Data reduction

The 28-s SWIR integration that captured Borrelly’s nucleus was acquired at a S/C range of 2910 km and a phase angle of  $41^\circ$ ; the raw frame is shown in Fig. 10. The Borrelly spectral data is in the bottom half of the top two quadrants. Nearer the top, stray sunlight, scattered into the keyhole, is seen as a sharply defined rectangle crossing the field. Electronic “ghosts” are also quite evident: most obvious are those residual signals that were transferred from the upper left to the lower left quadrant and less apparent

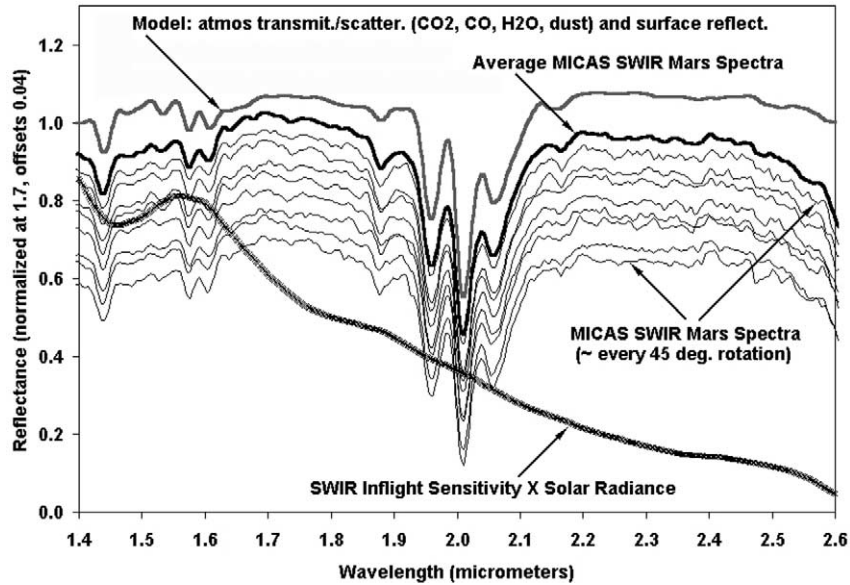


Fig. 9. Calibrated MICAS SWIR spectra of Mars from DS1 (average shown by bold black curve) compared with computationally modeled Mars spectrum (uppermost bold gray curve). Eight sets of Mars spectra (spaced every  $45^\circ$  of longitude) are offset below the average.

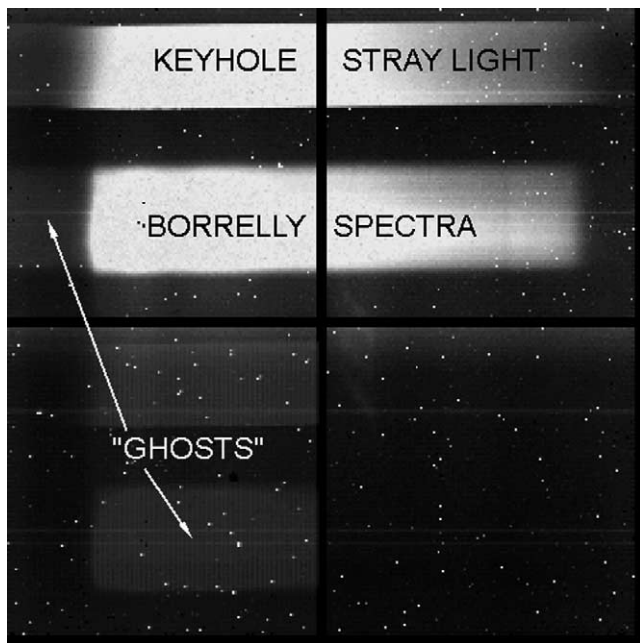


Fig. 10. Raw SWIR expose frame from the 28-s observation of the Borrelly nucleus observation (IRSTREAK1.PDS, see text).

from the upper right to the upper left quadrant (left of main data area). Scattered light can also be seen near the bottom edge of the main spectral swath near the bottom of the two upper quadrants. Using the procedures described in the previous section the data were processed to eliminate electronic ghosts, to model and subtract dark background, to correct for variation and non-linearity in sensitivity, despiked to remove “hot” and dead pixels, and to correct for the small optical shear. In addition scattered light was reduced by differencing the two SWIR observations (IRSTREAK1.PDS and IRSTREAK2.PDS) that were ac-

quired  $\sim 40$  s apart. Figure 11 shows the corrected data, still in image array format, but with lines inverted so that the spectral swaths correspond spatially to the adjacent image of the comet; this is the last and highest resolution VISCCD image (CCD\_NEAR\_1.PDS, see Soderblom et al., this issue). Unfortunately spectra for much of the nucleus were saturated at wavelengths  $\leq 2.3$   $\mu\text{m}$ ; but fortunately a few spectra (two at each end of the nucleus) are complete and unsaturated. The contribution from dust in the coma to these spectra is expected to be negligible.

Figure 12 shows the individual spectra extracted from Fig. 11 and calibrated in wavelength. The void in the central part of Fig. 11 (manifested as spectral gaps in Fig. 12) results from such saturation, worst where the swaths crossed the widest part of the nucleus. The units on the ordinate are DN (data number) accumulated over the full 28-s integration time. The product of the SWIR spectral sensitivity  $\times$  solar spectral radiance has not yet been divided out but is provided as a reference curve. Note that a spectrally gray target would parallel this curve. Two things are evident in the spectra as presented in this format:

- (1) relative to the reference curve (that represents a white Lambertian reflector) the Borrelly spectra are quite steep or “reddish,” and
- (2) an absorption feature near  $2.39$   $\mu\text{m}$  appears in all of the spectra.

Normally one would present and analyze these data in terms of absolute spectral radiance. This would be valuable for deriving and separating reflected and emitted components, fitting photometric models, and estimating normal spectral albedo. Unfortunately it is impossible to derive accurate absolute spectral radiance from these data alone; we



Fig. 11. Borrelly SWIR data frame of Fig. 10 after application of image-array corrections. The void in central part of spectral-spatial swath across the nucleus, represents saturated data. Lines of the spatial-spectral array have been inverted so that spectra correspond spatially to the MICAS VISCCD image shown at the left (CCD\_NEAR\_1.PDS, see Soderblom et al., this issue).

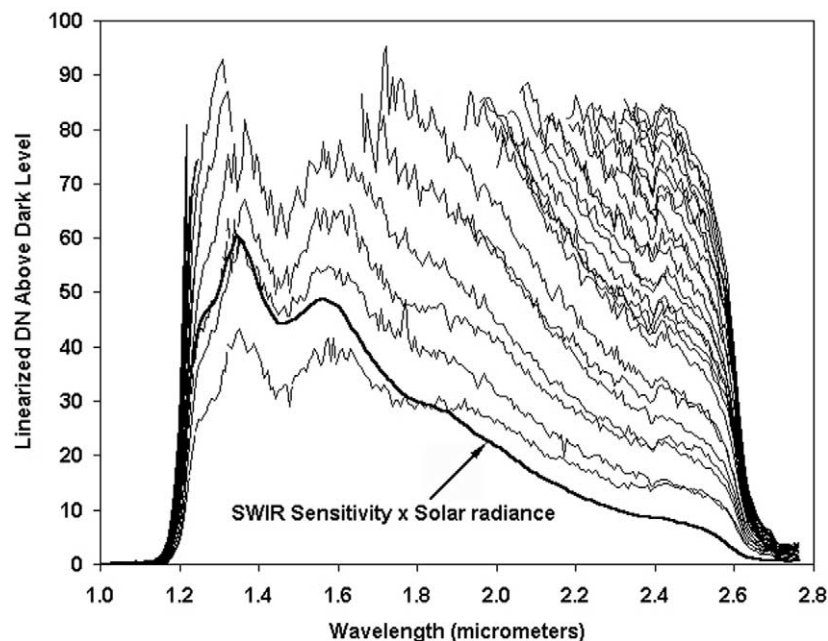


Fig. 12. Wavelength-calibrated spectra extracted from calibrated data set shown in Fig. 11. Data are in presented in linearized DN. The product of SWIR spectral response  $\times$  solar spectral radiance has not yet been removed, but is provided for comparison.

review the circumstances of the observation. During the VISCCD imaging sequence, the S/C pointing was continuously slewed to track the nucleus. On completion of the imaging sequence at  $-122$  s, the S/C was slewed to point the SWIR bore-sight ahead of the target and the S/C commanded to zero turn rate. At  $-117$  s the 28-s-long exposure was initiated. The nucleus therefore traversed the slit sometime between  $-117$  s and  $-89$  s. Assuming that the turn rate had been completely stopped, Borrelly's angular velocity of  $4.3$  mrad/s would have caused the nucleus to traverse the slit in  $\sim 2.5$  s. If the rate had not fully stopped before Borrelly entered the slit (which is more probable) the slit traverse time would have been greater and could have been somewhat  $> 2.5$  (s mrad)/s.

Assuming the effective integration was somewhere between  $2.5$  and  $5$  s we can do an *extremely* crude scaling of absolute photometry between the SWIR observations of Mars (shown in Fig. 9) and the Borrelly observations. Because the two observations (Mars and Borrelly) were acquired under very similar conditions (Mars:  $R_{\odot} \sim 1.38$  AU;

phase angle  $\sim 53^{\circ}$ ; Borrelly  $\sim 1.36$  AU; phase angle  $\sim 41^{\circ}$ ), rough scaling can be done rather simply. Mars filled approximately one spectral sample in the keyhole so the filling factor was about the same. We assume the integral disk phase function effects are also roughly the same. At  $2.35 \mu\text{m}$  the spectral data are complete for both: Mars generated  $\sim 2500$  DN/s whereas the average for the 45 Borrelly spectra is  $\sim 1600$  DN. Assuming the effective exposure time for Borrelly ranged between  $2.5$  and  $5$  s and an albedo for Mars  $R_n(2.35 \mu\text{m}) \sim 0.3$ , we can estimate the normal albedo for Borrelly of  $R_n(2.35 \mu\text{m})$  to be roughly  $0.06 \pm 0.02$ . The strong red slope of the Borrelly SWIR spectra shows the normal albedo in the visible would be roughly half these values. Adding another liberal factor of 2 in uncertainty from geometry (keyhole vs. slit) and from ignoring different phase function behaviors, we conservatively estimate the visible albedo from the SWIR data to be between  $0.01$  and  $0.08$ . This is crudely consistent with the  $0.03 \pm 0.01$  quoted by Soderblom et al. (2002) and Buratti et al. (this issue).

#### 4.2. Mapping surface temperature

Figure 13 shows the spectra of Fig. 12 after division by the product of the SWIR spectral sensitivity  $\times$  solar spectral irradiance; the spectra are normalized to unity at 2.359  $\mu\text{m}$ , chosen because all the Borrelly spectra are complete (unsaturated) at that wavelength and it is close to but short of the absorption feature at 2.39  $\mu\text{m}$ . The units are normalized radiance factor or  $I/F$  (defined as specific intensity divided by the incident solar flux;  $I/F = 1$  for a Lambertian disk illuminated and viewed normal to its surface). These are not yet normalized reflectance because thermal emission, quite evident beyond 2.2  $\mu\text{m}$ , has not yet been estimated and removed. Again only four spectra (two at each end) are complete and unsaturated over the entire wavelength range. The “nucleus large end” is the upper end as shown in Fig. 11. In Fig. 13 the spectra for the two ends appear to have slightly different slopes in reflectance but this conclusion is premature, again because differences in thermal emission at the two ends could be offsetting the normalization and affecting the slopes.

With respect to modeling the thermal emission in these data, we start from several considerations. Earth-based observations of the light curve by Lamy et al. (1998) and Mueller and Samarasingha (2001, 2002) show the nucleus rotation period to be  $25 \pm 0.5$  and  $26 \pm 1$  hr, respectively. At Borrelly’s distance from the Sun at the time of the encounter (1.362 AU), for a slow rotator the maximum temperature at the sub-solar point would be  $\sim 346$  K (assuming an emissivity = 0.9 and a bolometric Bond albedo = 0.02, cf. Buratti et al., this issue). Even for the highest-temperature cases, the thermal emission at wavelengths shorter than  $\sim 2$   $\mu\text{m}$  is negligible. In order to compute temperatures we need some way to scale the normalized SWIR spectra to absolute

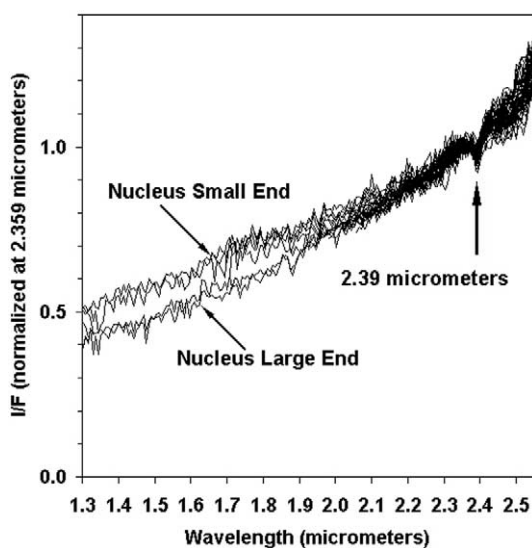


Fig. 13. Normalized spectra. The product of instrument spectral response  $\times$  solar spectral radiance has been divided out and results normalized at 2.359  $\mu\text{m}$  (see text). Nucleus large end is at the top and small end at the bottom in the image in Fig. 11.

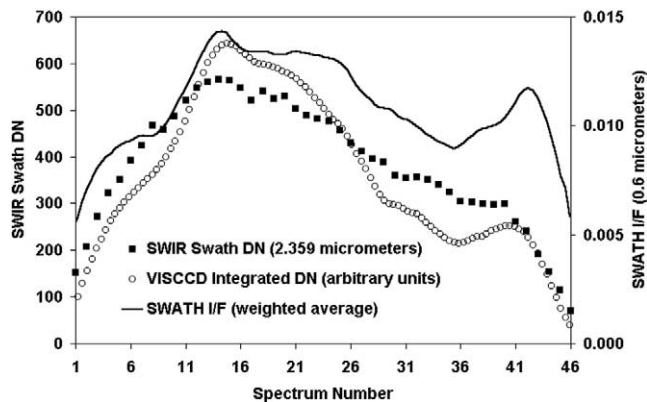


Fig. 14. Data sets used to scale normalized SWIR spectra (Fig. 13) to radiance flux. The linearized signal (DN) at 2.359  $\mu\text{m}$  for each SWIR swath is compared with a model of the integrated VISCCD DN estimated for that swath. The weighted average of  $I/F(0.6 \mu\text{m})$  was estimated for each swath (and is plotted against right axis, see text).

flux. We can estimate the necessary scaling factors from the photometric observations of the nucleus with the MICAS VISCCD camera whose effective wavelength is  $\sim 0.6$   $\mu\text{m}$ . Figure 14 compares the integrated 0.6  $\mu\text{m}$  brightness across each swath from VISCCD imaging (open circles) to the integral SWIR signal in each swath at 2.359  $\mu\text{m}$  (solid squares). The SWIR spectra are numbered from top-to-bottom: the first spectrum on the large end = 1 and the last on the small end = 46 (refer to Fig. 11). The difference in shape between the two curves probably arises from the difference in phase angle (CCD\_NEAR\_1  $\sim 51.6^\circ$  and IRSTREAK\_1  $\sim 41.0^\circ$ ) although it could be in part due to differences in reflectance slope. The SWIR data are normalized integrated values; they do not represent a simple average but a weighted average. Shown in Fig. 14 is the weighted average of  $I/F(0.6 \mu\text{m})$  derived from the VISCCD data for the spectrum for each swath. These values have also been adjusted from the phase angle of the image observation ( $51.6^\circ$ ) to that of the SWIR observation ( $41.0^\circ$ ), an increase of  $\sim 25\%$ .

Figure 15 shows the approach to fitting reflectance and thermal emission models to the four complete spectra available for the two ends of the nucleus. From Fig. 14 the weighted average of  $I/F$  at 0.6  $\mu\text{m}$  and  $41.0^\circ$  phase angle is  $\sim 0.005$  for both ends. In Fig. 15 we fit a linearly increasing reflectance models between 1.3 and 2.0  $\mu\text{m}$  (assuming negligible emission) and assume that this linear reflectance continues out to beyond 2.5  $\mu\text{m}$ . The vertical positions of the models were adjusted to  $I/F \sim 0.008$  at 1.3  $\mu\text{m}$  with the consideration that they must extrapolate in a reasonable way down to an  $I/F$  at 0.6  $\mu\text{m}$  of  $\sim 0.005$  (i.e.,  $I/F(1.3 \mu\text{m})/I/F(0.6 \mu\text{m}) \sim 1.6$ ).

Of course we do not know the slope of Borrelly’s reflectance curve (or  $I/F$  curve) between 0.6  $\mu\text{m}$  and 1.3  $\mu\text{m}$  but it cannot continue to zero at visible wavelengths; it must flatten out. Luu (1993) and Jewitt (2002) provide visible reflectance data for a variety of cometary nuclei. The combined mean of Jewitt’s classes “nuclei” and “dead comets”

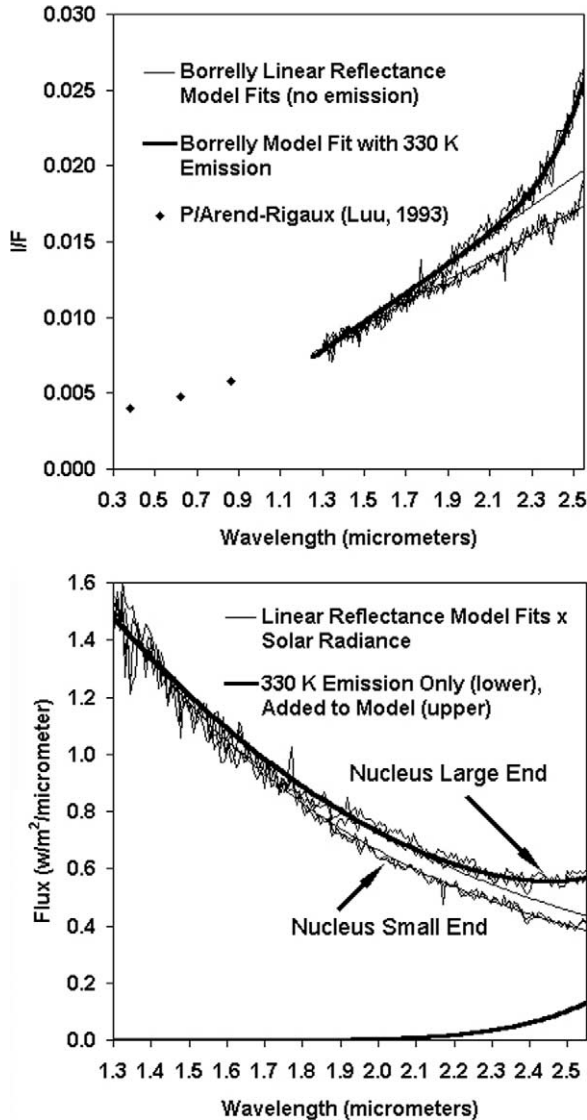


Fig. 15. Procedure to estimate thermal emission for SWIR spectra. *Top*: Linear reflectance models were fitted through each of the nucleus-end pairs of spectra. Spectra radiance adjusted to fit modeled  $I/F$ . Thermal emission estimated for nucleus large end is  $\sim 330$  K. Visible spectral reflectance for 49P/Arend–Rigaux nucleus provided for comparison. *Bottom*: Same data set and model fits as top in radiance units.

is  $\sim 10\%$  per  $0.1 \mu\text{m}$  (gradient of visible reflectivity) although the general range is from 0 to 20% per  $0.1 \mu\text{m}$ . Luu (1993) provides a visible reflectance spectrum for P/Arend–Rigaux extending from  $0.38$  to  $0.86 \mu\text{m}$  (exhibiting a slope near the mean of  $10\%$  per  $0.1 \mu\text{m}$ ). Although its nucleus is larger and less active, this mature short period comet is similar to P/Borrelly in its orbital and nucleus characteristics (Borrelly/Arend–Rigaux: period 6.86 yr/6.62 yr, eccentricity 0.624/0.612, perihelion = 1.359 AU/1.368 AU, period = 26 h/13.4 h, albedo 0.035/0.04, also see Millis et al., 1988). We have included a few points excerpted from the visible spectral reflectance of P/Arend–Rigaux in Fig. 15, scaled to 0.005 at  $0.6 \mu\text{m}$  simply to illustrate that our scaling of  $I/F$  from  $0.6$  to  $1.3 \mu\text{m}$  for Borrelly is reasonable.

In any case the value of  $I/F(1.3 \mu\text{m})$  for the SWIR spectra at Borrelly’s ends cannot be much greater than 0.008 because as we will discuss subsequently, raising this value much higher causes the model temperatures of the interior part of the nucleus to exceed maximum reasonable values. Thermal emission was then computed (assuming emissivity = 0.9 and absorption = 0.98). The model fits suggest

- (1) negligible measurable thermal emission for the two small-end spectra (temperature  $< 300$  K), and
- (2) substantial emission ( $\sim 330$  K) for the large-end spectra.

The bottom panel in Fig. 15 shows the same data and solutions in radiance units.

Using the approach described for Fig. 15 and the weighted average  $I/F(0.6 \mu\text{m})$  for each swath shown in Fig. 14, along with the assumption that the ratio  $I/F(1.3 \mu\text{m})/I/F(0.6 \mu\text{m}) \sim 1.6$ , models were computed for all 46 spectra (Fig. 16). Note that there was an error in Fig. 7 of Soderblom et al. (2002); the sequence of spectra was inverted and shown in the wrong order relative to the image. Figure 17 shows temperatures derived from those model fits; again the 46 spectra are numbered from top to bottom (large end to small end in Figs. 11 and 16). A water ice spectrum is included for comparison in Fig. 16; as noted by Soderblom et al. (2002) there is no detectable evidence of absorption due to exposed water ice in any of the spectra. The spectra are offset from one another for clarity by increments of  $\pm 0.05$  in the ordinate direction.

The dark, hot, dry nature of the surface of Borrelly’s nucleus is not surprising. Throughout the 1980’s cometary nuclei observed near Earth in the near infrared and visible consistently showed very low albedo surfaces (0.01–0.04) with high temperatures (300–400 K depending on heliocentric range) close to those expected in equilibrium with solar insolation and far above temperatures expected for subliming water ice of  $\sim 220$  K (Veeder and Hanner, 1981; Tokunaga and Hanner, 1985; Brooke and Knacke, 1986; Veeder et al., 1987; Campins et al., 1987; Hanner et al., 1987). Similar high temperatures, close to equilibrium, were observed for the nucleus of comet Halley from the VEGA-1 flyby. Combes et al. (1986) and Emerich et al. (1987) estimated surface temperatures  $> 360$  K and as high as 420 K from the IKS infrared spectrometer data. Keller et al. (1986) and Sagdeev et al. (1986) reported albedos near 0.04 from Giotto and VEGA imaging experiments, respectively.

The hot dry surface and lack of water ice features is also consistent with estimates that only a few percent of the surface is actively subliming at perihelion (Lamy et al., 1998; Schleicher et al., 2003; Weaver et al., 2003). Furthermore, because the footprint of each spectrum is a swath that runs from sun-facing limb to the opposite terminator, the hot dry regions must dominate the spectrum. The regions that are cold (say  $\sim 220$  K) where ice is actively subliming could be highly diluted in the spectra.

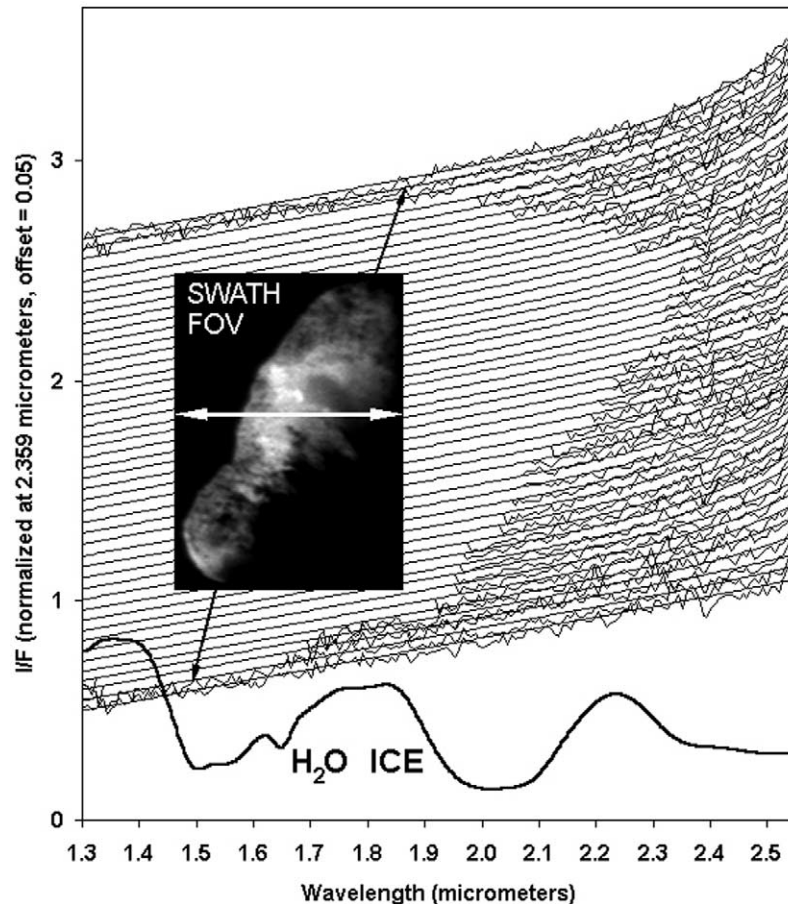


Fig. 16. Each of 46 spectra covers a swath 160-m (tall in this view) across the width of the nucleus (shown schematically by swath FOV arrow). Model fits for reflectance and thermal emission for each spectrum are shown as smooth curves. Spectra are normalized at 2.359  $\mu\text{m}$  and offset from one another by increments of 0.05 for clarity (offset = 0 for bottom spectrum). Also included is a spectrum for water ice (50- $\mu\text{m}$  grains). Borrelly's strongly red-sloped spectra show no trace of water ice.

Inspection of the image in Fig. 17 shows that the small end spectra were acquired very close to the terminator on that end of the nucleus. It is likely that the fall off in temperature at the small end is simply due to fall off in insolation. The digital topographic models provided by Kirk et al. (this issue) and Oberst et al. (this issue) can be used to predict temperatures for the nucleus surface. However the SWIR data were taken at phase angles  $\sim 41^\circ$  and the topographic models were generated from data at phase angles  $> 52^\circ$ . Hence the topographic models do not contain the hot bright limb that was included in the SWIR data and that the limb will dominate the weighted average SWIR spectra. Extrapolation of the topographic models into this region and model fitting to the SWIR observations is possible but remains for future work.

#### 4.3. Red slope

Figure 18 compares spectra of the ends of the Borrelly nucleus (emission subtracted) with other strongly red-sloped Solar System objects (Bell et al., 1988; Hiroi et al., 2001). The slight difference in slope in the spectra for the two ends

remains after removal of the thermal emission contribution for the hotter, large end. However this slope difference is at the limit of the accuracy of the data.

Borrelly's near-IR spectral reflectance is among the steepest or reddest observed Solar System objects. From Fig. 18 the H-K for Borrelly is  $\sim 0.43$  and, by extrapolation to 1.25  $\mu\text{m}$ , J-K is  $\sim 0.82$ . Surfaces of some comets have been thought to be dark and red, similar in infrared color to D-type asteroids, since the mid-1980s. Brooke and Knacke (1986) and Veeder et al. (1987) estimated the J-K color for the nucleus of Comet P/Arend-Rigaux to be  $\sim 0.6$  similar only to very red D-asteroids (cf. Veeder et al., 1982, 1983). Cruikshank et al. (1985) and Brooke et al. (1985) reported J-K values of 0.6–0.7 for Halley's nucleus. Borrelly is among the very reddest objects such as 1999 LD<sub>31</sub>, a possible inactive cometary nucleus, for which Harris et al., 2001 found J-K  $\sim 0.8$ .

Spectral D-type asteroids are typically the "reddest" of asteroids and are thought to be composed of dark, organic-rich, carbon-rich, volatile-rich materials (Gaffey et al., 1993). Figure 18 shows that compared to Borrelly in the 1.3–2.5  $\mu\text{m}$  region, the red D-asteroids 336 Lacadiera and

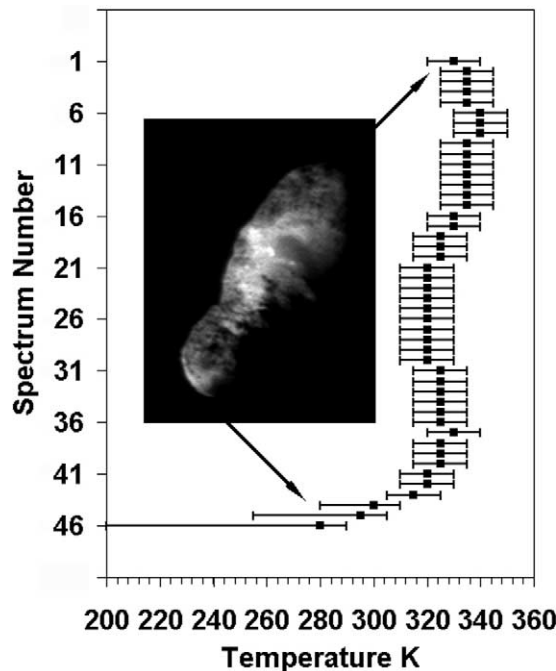


Fig. 17. Temperature mapped from model fits to 46 swaths shown in Fig. 16. The temperatures represent the flux-weighted average for each swath (see text).

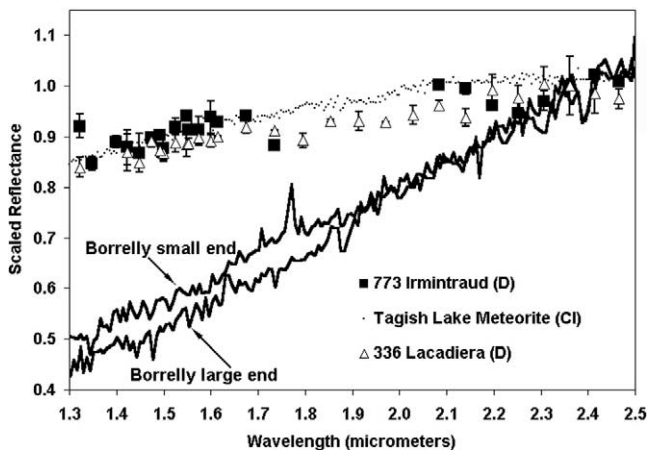


Fig. 18. Borrelly's normalized reflection spectra for ends of nucleus (emission removed) compared with steep-slope infrared spectra of two asteroids and a meteorite.

773 Irmintraud seem almost flat. Similarly, the spectra of the volatile-rich carbonaceous chondrite Tagish lake, which is thought to be the best meteoritic analogue for primitive asteroids (Hiroi et al., 2001), is substantially less red than Borrelly. There is no evidence of an absorption at 2.39  $\mu\text{m}$  in its spectrum; the much lower resolution spectra of the D-type asteroids not as definitive, but there is little evidence for an absorption at this wavelength. The evidence from these data show Borrelly does not have spectral similarities to primitive asteroids or volatile-rich meteorites. Borrelly's origin, composition, and evolution are much different from materials in our meteorite collections, or even the dark, primitive

asteroids of the outer asteroid belt. The lack of water ice is also consistent with the strong red-ward slope in the near infrared. Many Solar System objects that are very red in visible wavelengths do not show strong red slopes in the SWIR due to the presence of water.

#### 4.4. Absorption feature

The question remains as to the source of the 2.39  $\mu\text{m}$  feature that is present in every one of the discrete spectra of Borrelly's nucleus. This feature has the potential of serving as an identifying signature that could distinguish extinct comet nuclei from other types of dark, icy objects in the outer Solar System. Accordingly, we have looked for it in published and unpublished spectra of these objects. It is not present in spectra of those outer planet satellites that have been observed, including Callisto, Himalia, Umbriel, Phoebe and the dark side of Iapetus (Owen et al., 1999, 2001, 2002 (Unpublished spectra of Callisto and Umbriel); Geballe et al., 2002). It is also missing from spectra of dark asteroids, including three of Jupiter's Trojans (Luu et al., 1994; Dumas et al., 1998; Cruikshank et al., 2001). Upper limits vary depending on the quality of the spectra. For example, the spectrum of Comet Hale–Bopp that reveals the presence of water ice is too noisy at 2.39  $\mu\text{m}$  to show this feature unless it were as strong as the ice absorptions (Davies et al., 1997).

In fact, the only dark, icy object that exhibits discrete absorptions not due to water ice is the Centaur 5145 Pholus (Luu et al., 1994; Cruikshank et al., 1998). However, the prominent absorption on Pholus is at 2.27  $\mu\text{m}$ , not 2.39  $\mu\text{m}$ . The identification of the Pholus feature is not secure, but it may be caused by frozen methanol and/or a photolytic product of methanol (Cruikshank et al., 1998), or a mixture of hydrocarbons similar to those present in a high-bitumen sample of tar sand (Luu et al., 1994). In addition to the mismatch in wavelength, methanol and its products seem unlikely candidates for the warm surface of Borrelly. Bitumen offers better stability but none of the published spectra exhibit discrete features at 2.39  $\mu\text{m}$ . The absorption in this spectral region typically peaks at 2.3  $\mu\text{m}$  and is attributed to overtones of  $\text{CH}_3$  bending and stretching modes (Cloutis, 1989; Cloutis et al., 1994).

Figure 19 compares the reduced Borrelly spectra to several organic molecules that have been suggested as candidates for cometary surface components. The first is POM,  $(\text{HCHO})_n$  (polyoxymethylene or paraformaldehyde), that is a linear polymer of trioxane and was identified by Huebner (1987) and Mitchell et al. (1987) as a component of Halley's coma dust from Giotto measurements. However POM does not show a feature at the location of the 2.39  $\mu\text{m}$  Borrelly absorption. Interestingly the spectra of the two nitrogen-bearing organics in Fig. 19, both exhibit absorption features near this spectral position. The first, hexamethylenetetramine (HMT) was discussed by Cruikshank et al. (1998) as a possible candidate for absorption features seen in Centaur 5145 Pholus. Bernstein et al. (1995) de-

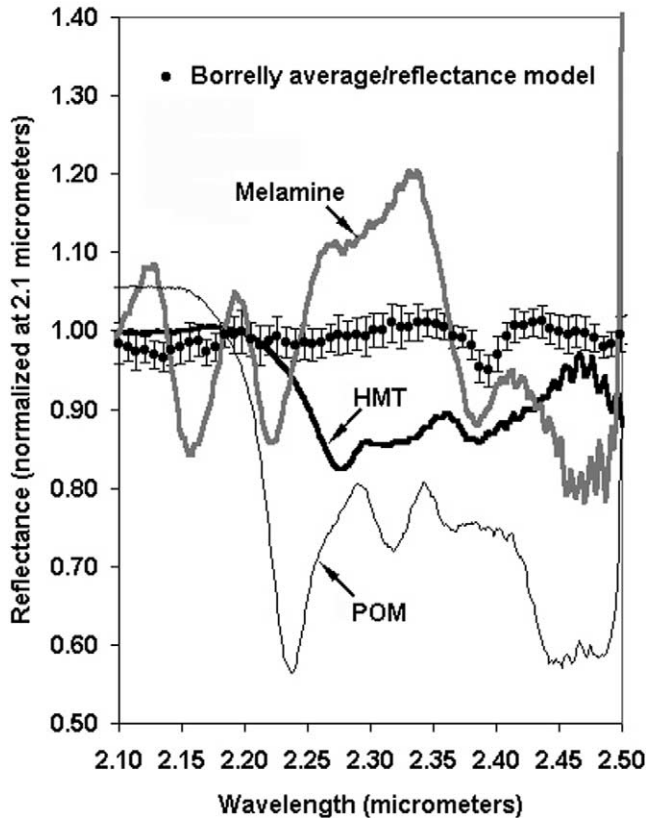


Fig. 19. Comparison Borrelly nucleus spectrum with some candidate materials. The Borrelly spectra have had emission subtracted and then divided by the linear continuum models (cf. Fig. 15). The two nitrogen-bearing molecules (HMT or hexamethylenetetramine and melamine) show a feature near the position of the Borrelly feature. POM (polyoxymethylene or paraformaldehyde) does not show a feature at this wavelength.

scribe the chemical sequence by which HMT is produced from the reaction of formaldehyde and ammonia. The other nitrogen-bearing organic is Melamine ( $C_3H_6N_6$ ), a trimer of cyanamide ( $CH_2N_2$ ) that has been long known to exist in interstellar clouds (cf. Mann and Williams, 1980). Melamine would be quite stable on the surfaces of mature short-period comets (melting point  $\sim 345$  C). However, both of these candidates exhibit absorptions at other wavelengths that are not present in the Borrelly spectra. We have also researched compilations of mineral spectra, again without finding a match. To summarize, we are not yet able to identify the species responsible for the 2.39  $\mu$  feature, and we are therefore unable to establish it as a definitive marker for comet nuclei. We encourage observers of dark, icy objects in the outer Solar System to keep this absorption in mind.

## 5. Conclusions and summary

Observations of Comet 19P/Borrelly's nucleus with the MICAS Short-wavelength infrared imaging spectrometer aboard Deep Space 1 have yielded unique spectroscopic information for a cometary nucleus. Analysis of the data reveals the following:

- The short-wavelength infrared spectra of Borrelly's nucleus show a steep red slope spectral reflectance from 1.3–2.5  $\mu$ m. The two ends of the nucleus may exhibit slight differences in reflectance slope.
- Borrelly's J–K ( $\sim 0.82$ ) and H–K ( $\sim 0.43$ ) colors are among the very reddest D-type asteroids and cometary nuclei so far observed.
- The SWIR spectra indicate a hot, dry surface. Model temperatures continuously range from  $\leq 300$  K near the terminator to  $\sim 345$  K in the central regions to  $\sim 330$  K near the large end of the nucleus. These temperatures are close to those expected for a slow-rotating object in thermal equilibrium with incident solar radiation.
- No trace of spectral features associated with  $H_2O$  ice is found in the spectra. This taken with the high temperature is consistent with  $\sim 90\%$  or more of the surface area being inactive with active sublimation occurring only on a small fraction.
- A 0.1- $\mu$ m wide absorption feature at 2.39  $\mu$ m persists in all of the 46 SWIR spectra of the surface. Such features are characteristic of a variety of organic compounds proposed as candidates for cometary surfaces. Some nitrogen-bearing organic molecules show a feature at this wavelength. However they also show numerous other absorptions not seen in the spectra. No specific identification can be made at this time.

## Acknowledgments

We thank Jacques Crovisier, Dale Cruikshank, Lisa Gaddis, and Jeffrey Johnson for insightful reviews. This research was completed under NASA funding from the New Millennium Deep Space 1 Project conducted by the Jet Propulsion Laboratory of the California Institute of Technology.

## References

- Beauchamp, P.M., Brown, R.H., Bruce, C.F., Chen, G.-S., Chrisp, M.P., Fraschetti, G.A., Krabach, T.N., Petrick, S.W., Rodgers, D.H., Rodriguez, J., Soll, S.L., Vaughan, A.H., Soderblom, L.A., Sandel, B.R., Yelle, R.V., 1994. Pluto integrated camera spectrometer (PICS) instrument. In: Proc. SPIE, Vol. 2214, pp. 269–277.
- Bell, J.F., Owensby, P.D., Hawke, B.R., Gaffey, M.J., 1988. The 52-color asteroid survey: final results. In: Proc. Lunar Planet. Sci. Conf. 19th, p. 57. Abstract.
- Bernstein, M.P., Sandford, S.A., Allamandola, L.J., Chang, S., Scharberg, M.A., 1995. Organic compounds produced by photolysis of realistic interstellar and cometary ice analogs containing methanol. *Astrophys. J.* 454, 327.
- Brooke, T.Y., Knacke, R.F., 1986. The nucleus of Comet P/Arend–Rigaux. *Icarus* 67, 80–87.
- Brooke, T.Y., Knacke, R., Wehinger, P.A., Wyckoff, S., Foltz, C., Heller, C., Wagner, M., Schleicher, D., Festou, M., 1985. Periodic Comet Halley (1982i). *IAU Circ.* 4041, 2.
- Campins, H., A'Hearn, M.F., McFadden, L., 1987. The bare nucleus of Comet Neujmin 1. *Astrophys. J.* 316, 847–857.
- Cloutis, E.A., 1989. Spectral reflectance properties of hydrocarbons: remote-sensing implications. *Science* 245, 165–168.

- Cloutis, E.A., Gaffey, M.J., Moslow, T.F., 1994. Spectral reflectance properties of carbon-bearing minerals. *Icarus* 107, 275–287.
- Cohen, M., Witteborn, F.C., Walker, R.G., Bregman, J.D., Wooden, D.H., 1995. Spectral irradiance calibration in the infrared. IV. 1.2–35 micron spectra of six standard stars. *Astron. J.* 110, 275.
- Combes, M., Moroz, V.I., Crifo, J.F., Lamarre, J.M., Charra, J., Sanko, N.F., Soufflot, A., Bibring, J.P., Cazes, S., Coron, N., Crovisier, J., Emerich, C., Encrenaz, T., Gispert, R., Grigoryev, A.V., Guyot, G., Krasnopolsky, V.A., Nikolsky, Y.V., Rocard, F., 1986. Infrared sounding of Comet Halley from VEGA 1. *Nature* 321, 266–268.
- Cruikshank, D.P., Hartmann, W.K., Tholen, D.J., 1985. Colour, albedo and nucleus size of Halley's comet. *Nature* 315, 122–124.
- Cruikshank, D.P., Roush, T.L., Bartholomew, M.J., Geballe, T.R., Pendleton, Y.J., White, S.M., Bell, J.F., Davies, J.K., Owen, T.C., de Bergh, C., Tholen, D.J., Bernstein, M.P., Brown, R.H., Tryka, K.A., Dalle Ore, C.M., 1998. The composition of Centaur 5145 pholus. *Icarus* 135, 389–407.
- Cruikshank, D.P., Dalle Ore, C.M., Roush, T.L., Geballe, T.R., Owen, T.C., de Bergh, C., Cash, M.D., Hartmann, W.K., 2001. Constraints on the composition of Trojan Asteroid 624 Hektor. *Icarus* 153, 348–360.
- Davies, J.K., Roush, T.C., Cruikshank, D.P., Bartholomew, M.J., Geballe, T.R., Owen, T., de Bergh, C., 1997. The detection of water ice in Comet Hale-Bopp. *Icarus* 127, 238–245.
- Dumas, C., Owen, T., Barucci, M.A., 1998. Near-infrared spectroscopy of low-albedo surfaces of the Solar System: search for the spectral signature of dark material. *Icarus* 133, 221–232.
- Emerich, C., Lamarre, J.M., Moroz, V.I., Combes, M., Sanko, N.F., Nikolsky, Y.V., Rocard, F., Gispert, R., Coron, N., Bibring, J.P., Encrenaz, T., Crovisier, J., 1987. Temperature and size of the nucleus of Comet p/Halley deduced from IKS infrared VEGA-1 measurements. *Astron. Astrophys.* 187, 839–842.
- Gaffey, M.J., Burbine, T.H., Binzel, R.P., 1993. Asteroid spectroscopy: progress and perspectives. *Meteoritics* 28, 161–187.
- Geballe, T.R., Dalle Ore, C.M., Cruikshank, D.P., Owen, T.C., 2002. The 1.95–2.50  $\mu\text{m}$  spectrum of J6 Himalia. *Icarus* 159, 542–544.
- Hanner, M.S., Newburn, R.L., Spinrad, H., Veeder, G.J., 1987. Comet Sugano-Saigusa-Fujikawa (1983V)—a small, puzzling comet. *Astron. J.* 94, 1081–1087.
- Harris, A.W., Delbo, M., Binzel, R.P., Davies, J.K., Roberts, J., Tholen, D.J., Whiteley, R.J., 2001. Visible to thermal-infrared spectrophotometry of a possible inactive cometary nucleus. *Icarus* 153, 332–337.
- Hiroi, T., Zolensky, M.E., Pieters, C.M., 2001. The Tagish lake meteorite: a possible sample from a D-type asteroid. *Science* 293, 2234–2236.
- Huebner, W.F., 1987. First polymer in space identified in Comet Halley. *Science* 237, 628–630.
- Jewitt, D.C., 2002. From Kuiper belt object to cometary nucleus: the missing ultrared matter. *Astron. J.* 123, 1039–1049.
- Keller, H.U., Arpigny, C., Barbieri, C., Bonnet, R.M., Cazes, S., Coradini, M., Cosmovici, C.B., Delamere, W.A., Huebner, W.F., Hughes, D.W., Jamar, C., Malaise, D., Reitsema, H.J., Schmidt, H.U., Schmidt, W.K.H., Seige, P., Whipple, F.L., Wilhelm, K., 1986. First Halley multicolour camera imaging results from Giotto. *Nature* 321, 320–326.
- Lamy, P.L., Toth, I., Weaver, H.A., 1998. Hubble Space Telescope observations of the nucleus and inner coma of Comet 19P/1904 Y2 (Borrelly). *Astron. Astrophys.* 337, 945–954.
- Luu, J.X., 1993. Spectral diversity among the nuclei of comets. *Icarus* 104, 138–148.
- Luu, J., Jewitt, D., Cloutis, E., 1994. Near-infrared spectroscopy of primitive Solar System objects. *Icarus* 109, 133–144.
- Mann, A.P.C., Williams, D.A., 1980. A list of interstellar molecules. *Nature* 283, 721–725.
- Millis, R.L., A'Hearn, M.F., Campins, H., 1988. An investigation of the nucleus and coma of Comet P/Arend-Rigaux. *Astrophys. J.* 324, 1194–1209.
- Mitchell, D.L., Lin, R.P., Anderson, K.A., Carlson, C.W., Curtis, D.W., Korth, A., Reme, H., Sauvaud, J.A., D'Uston, C., Mendis, D.A., 1987. Evidence for chain molecules enriched in carbon, hydrogen, and oxygen in Comet Halley. *Science* 237, 626–628.
- Mueller, B., Samarasinha, N., 2001. Lightcurve observations of 19P/Borrelly. *Bull. Am. Astron. Soc.* 33, 1090.
- Mueller, B.E.A., Samarasinha, N.H., 2002. Visible lightcurve observations of Comet 19P/Borrelly. *Earth Moon Planets* 90, 463–471.
- Owen, T.C., Cruikshank, D.P., Dalle Ore, C.M., Geballe, T.R., Roush, T.L., de Bergh, C., 1999. Detection of water ice on Saturn's satellite Phoebe. *Icarus* 140, 379–382.
- Owen, T.C., Cruikshank, D.P., Dalle Ore, C.M., Geballe, T.R., Roush, T.L., de Bergh, C., Meier, R., Pendleton, Y.J., Khare, B.N., 2001. Decoding the domino: the darkside of Iapetus. *Icarus* 149, 160–172.
- Sagdeev, R.Z., Szabo, F., Avanesov, G.A., Cruvellier, P., Szabo, L., Szego, K., Abergel, A., Balazs, A., Barinov, I.V., Bertaux, J.-L., Blamont, J., Detaille, M., Demarelis, E., Dul'nev, G.N., Endroczy, G., Gardos, M., Kanyo, M., Kostenko, V.I., Krasikov, V.A., Nguyen-Trong, T., Nyitrai, Z., Reny, I., Rusznyak, P., Shamis, V.A., Smith, B., Sukhanov, K.G., Szabo, F., Szalai, S., Tarnopolsky, V.I., Toth, I., Tsukanova, G., Valnick, B.I., Varhalmi, L., Zaiko, Yu.K., Zatsopin, S.I., Ziman, Ya.L., Zsenei, M., Zhukov, B.S., 1986. Television observations of Comet Halley from VEGA spacecraft. *Nature* 321, 262–266.
- Schleicher, D.G., Woodney, L.M., Millis, R.L., 2003. Comet 19P/Borrelly at multiple apparitions: seasonal variations in gas production and dust morphology. *Icarus* 162, 415–442.
- Soderblom, L.A., Yelle, R.V., 2001. Near-infrared reflectance spectroscopy of Mars (1.4–2.6  $\mu\text{m}$ ) from the New Millennium Deep Space 1 miniature integrated camera and spectrometer (MICAS). In: *Proc. Lunar Planet. Sci. Conf.* 32nd, p. 1473. Abstract.
- Soderblom, L.A., Beauchamp, P.M., Chen, G.-S., Elliott, S.T., Fraschetti, G.A., Lee, M., Pain, B., Petrick, S.W., Ringold, P.G., Rodgers, D.H., Sandel, B.R., Soll, S.L., Thomas, D.A., Wang, D., 2000. Miniature integrated camera spectrometer (MICAS) technology validation report. In: *Extended Abstracts and Fact Sheets: Deep Space 1 Technologies, Deep Space 1 Technology Validation Symposium, February 8–9, 2000, Pasadena CA.*
- Soderblom, L.A., Becker, T.L., Bennett, G., Boice, D.C., Britt, D.T., Brown, R.H., Buratti, B.J., Isbell, C., Giese, B., Hare, T., Hicks, M.D., Howington-Kraus, E., Kirk, R.L., Lee, M., Nelson, R.M., Oberst, J., Owen, T.C., Sandel, B.R., Rayman, M.D., Stern, S.A., Thomas, N., Yelle, R.V., 2002. Observations of Comet 19P/Borrelly by the miniature integrated camera and spectrometer aboard Deep Space 1. *Science* 296, 1087–1091.
- Tokunaga, A.T., Hanner, M.S., 1985. Does Comet P/Arend-Rigaux have a large dark nucleus? *Astrophys. J.* 296, L13–L16.
- Veeder, G.J., Hanner, M.S., 1981. Infrared photometry of Comets Bowell and P/Stephan-Oterma. *Icarus* 47, 381–387.
- Veeder, G.J., Matson, D.L., Kowal, C., 1982. Infrared JHK photometry of asteroids. *Astron. J.* 87, 834–839.
- Veeder, G.J., Matson, D.L., Hoover, G., Kowal, C., 1983. Infrared (JHK) photometry of asteroids. II. *Astron. J.* 88, 1060–1063.
- Veeder, G.J., Hanner, M.S., Tholen, D.J., 1987. The nucleus of Comet P/Arend-Rigaux. *Astron. J.* 94, 169–173.
- Weaver, H.A., Stern, S.A., Parker, J.W., 2003. HST/STIS observations of Comet 19P/Borrelly during the Deep Space 1 Encounter. *Astron. J.* 126, 444–451.